

# Tape-time processing: Kinetics and mechanisms of native oxidation of transition metal dichalcogenides

## ZrS<sub>x</sub>Se<sub>2-x</sub> and MoS<sub>2</sub>

*Seong Soon Jo<sup>1</sup>, Akshay Singh<sup>1†</sup>, Liqiu Yang<sup>2</sup>, Subodh C. Tiwari<sup>2</sup>, Sungwook Hong<sup>3</sup>, Aravind Krishnamoorthy<sup>2</sup>, Maria Gabriela Sales<sup>4</sup>, Sean M. Oliver<sup>6,7</sup>, Joshua Fox<sup>5</sup>, Randal L. Cavaleiro<sup>5</sup>, David W. Snyder<sup>5</sup>, Patrick M. Vora<sup>6,7</sup>, Stephen J. McDonnell<sup>4</sup>, Priya Vashishta<sup>2</sup>, Rajiv K. Kalia<sup>2</sup>, Aiichiro Nakano<sup>2</sup>, Rafael Jaramillo<sup>1\*</sup>*

1. Department of Materials Science and Engineering, Massachusetts Institute of Technology,  
Cambridge, MA 02139, USA

2. Collaboratory for Advanced Computing and Simulation, University of Southern California,  
Los Angeles, CA 90089, USA

3. Department of Physics and Engineering, California State University, Bakersfield, Bakersfield,  
CA 93311, USA

4. Department of Materials Science and Engineering, University of Virginia, Charlottesville, VA  
22904, USA

5. Electronic Materials and Devices Department, Applied Research Laboratory and 2-Dimensional Crystal Consortium, Materials Research Institute, Pennsylvania State University, University Park, PA 16802, USA

6. Department of Physics and Astronomy, George Mason University, Fairfax, VA 22030, USA

7. Quantum Materials Center, George Mason University, Fairfax, VA 22030, USA

† Present address: Department of Physics, Indian Institute of Science, Bengaluru, Karnataka, 560012, India

**\* Corresponding Author**

E-mail: [rjaramil@mit.edu](mailto:rjaramil@mit.edu)

**Abstract**

A thorough understanding of the processing and properties of native oxides is essential for designing semiconductor devices. This is no less true for nanomaterials than it is for legacy semiconductors such as silicon, for which control and understanding of the native oxide was a seminal achievement of 20<sup>th</sup> century materials science. Layered transition metal dichalcogenides nominally have inert, fully-passivated surfaces, but it is well-known that this is an oversimplification and that many TMDs oxidize readily. Here we report on experiments and simulations that reveal the rate and mechanism of oxidation of MoS<sub>2</sub> and ZrS<sub>x</sub>Se<sub>2-x</sub> alloys in laboratory conditions. We find that MoS<sub>2</sub> surfaces are indeed stable, with no oxidation for up to a year exposure. In contrast, ZrS<sub>x</sub>Se<sub>2-x</sub> alloys oxidize spontaneously and the oxide growth is not self-limited. Oxidation proceeds by Zr-O bond switching that collapses the van der Waals gaps, and is facilitated by progressive redox transitions of the chalcogen. In contrast, the MoS<sub>2</sub> surface remains

inert due to energetically-unfavorable oxygen adsorption. Our results provide quantitative and conceptual guidance for designing and processing semiconductor devices based on  $\text{MoS}_2$  and  $\text{ZrS}_x\text{Se}_{2-x}$ , and identify the atomistic-scale mechanisms of bonding and phase transformations in layered materials with competing anions.

**Keyword:** Transition metal dichalcogenides, Native oxidation, Kinetics, Spectroscopic ellipsometry, Reactive molecular dynamics simulations, ReaxFF reactive force field

Transition metal dichalcogenides (TMDs) are of widespread current interest for fundamental studies and technological applications, from nanoscale tribology to quantum computing. As interest grows for applications in microelectronics, photonics, and optoelectronics, so too does the importance of developing predictive materials processing methods.<sup>1-6</sup> One of the most critical issues for any functional material is the formation and properties of the native oxide. The history of silicon microelectronics illustrates the importance of understanding and controlling native oxides.<sup>7</sup> Examples can also be easily found for lesser-developed semiconductors, including chalcogenides.<sup>8-10</sup> The stability of TMDs has been studied in ambient conditions and various harsh and oxidizing environments.<sup>11</sup> Oxidation has been observed to initiate at defects, and may be facilitated by organic adsorbates.<sup>8,10,12</sup> It is also known that monolayers are less stable than few-layer and bulk crystals, that stability against oxidation in air increases as the chalcogen element changes from Te, to Se, to S, and that TMDs including group 4 transition metals are particularly unstable in air.<sup>8,13,14</sup> The kinetics of oxide formation in ambient conditions will be important for device processing and technology development.<sup>9</sup>

Here we report on the rate of native oxidation in ambient conditions of freshly-cleaved surfaces of bulk single crystals of  $\text{ZrS}_x\text{Se}_{2-x}$  alloys and  $\text{MoS}_2$ ; in **Fig. 1** we present photographs of several of the crystals studied, and a schematic of the experimental procedure. We find that the Zr-based materials oxidize readily, with the rate increasing with Se content in the alloy. Meanwhile,  $\text{MoS}_2$  seems to oxidize not at all in air on a laboratory time scale. We use first principles-validated reactive molecular dynamics (RMD) simulations to elucidate the atomistic mechanism of oxidation. We find that oxygen moves readily into the  $\text{ZrS}_2$  crystal lattice by a mechanism of Zr-O bond switching, and that the rate-limiting steps for native oxidation are the formation and out-diffusion of  $\text{SO}_2$ . In contrast, we find that surface oxidation is kinetically-limited in  $\text{MoS}_2$  due to a

large O<sub>2</sub> dissociative adsorption barrier, even though chemisorbed oxygen is thermodynamically stable.<sup>15</sup>

## Results and Discussion

In **Fig. 2** we present the imaginary component of the effective dielectric constant ( $\epsilon_2^{\text{eff}}$ ) measured on select ZrS<sub>x</sub>Se<sub>2-x</sub> alloys as a function of time after cleaving, measured by spectroscopic ellipsometry (SE). SE can measure oxide formation with sub-nm and single-monolayer resolution. SE measures the complex reflectance ratio  $\rho = \frac{r_p}{r_s} = \tan \Psi e^{i\Delta}$ ;  $r_p$  and  $r_s$  are the amplitude Fresnel reflection coefficients for p- and s-polarized light, respectively, and  $\rho$  is parameterized by the ellipsometry amplitude  $\tan\Psi$  and angle  $\Delta$ . The effective dielectric constant is determined by calculating the complex dielectric constant ( $\epsilon^{\text{eff}}$ ) by direct inversion of SE data,  $\rho$  and the angle of incidence ( $\Phi$ ):  $\epsilon^{\text{eff}} = \sin^2(\Phi) \left( 1 + \tan^2(\Phi) \left( \frac{1-\rho}{1+\rho} \right)^2 \right)$ . This analysis is accurate only for a uniform, semi-infinite sample with an intimate and smooth sample-air interface, hence the qualifier “effective”. The time-dependence of the data in **Fig. 2** is a straightforward clue that the actual sample structure is more complicated, and is changing in time as the sample is exposed to air. Comparing the results for ZrSe<sub>2</sub> (**Fig. 2a**) to the results for ZrS<sub>2</sub> (**Fig. 2c**), we see that the sulfide is more air-stable. The peaks in the  $\epsilon_2^{\text{eff}}$  spectra derive from the lowest-lying direct, allowed optical transitions and excitons ( $X_\Gamma, X_L, X_A$ ), which blue-shift with sulfur content across the ZrS<sub>x</sub>Se<sub>2-x</sub> series, as we report in detail elsewhere.<sup>16</sup>

In **Fig. 3** we show SE time-series data recorded after cleaving a fresh surface of MoS<sub>2</sub>. In contrast to the results for ZrS<sub>x</sub>Se<sub>2-x</sub>, the results for MoS<sub>2</sub> show no apparent change, even after many days of exposure. This suggests that a pristine MoS<sub>2</sub> surface does not spontaneously oxidize in air on

laboratory time scales. Below we analyze and rule out an alternative explanation, that an ultra-thin and kinetically-stable native oxide forms rapidly upon air exposure, undetected by our SE measurements.

If freshly-cleaved MoS<sub>2</sub> does maintain a pristine surface in air, then the sample measured by SE is well-modeled as a semi-infinite sample with an intimate and smooth air interface. In this case, the effective dielectric constant is an accurate estimate of the optical properties of the material. In **Fig. 3a** we show the complex dielectric constant ( $\epsilon_1 - i\epsilon_2$ ), and in **Fig. 3b** we show the complex refractive index ( $n - ik$ ). The optical transitions characteristic of MoS<sub>2</sub> excitons A ( $\approx 1.8$  eV), B ( $\approx 2.1$  eV), C ( $\approx 2.7$  eV) and D ( $\approx 3.1$  eV) are clearly observed in the loss spectra ( $\epsilon_2$  and  $k$ ). We note the small loss coefficient,  $k < 0.05$ , for photon energy near and below the indirect band gap of 1.29 eV. This value is lower than our previously-reported value of  $k \approx 0.2$ , which we determined from SE measurements on geological crystals from the same batch but without cleaving.<sup>5</sup> This illustrates the sensitivity of SE to surface conditions, including roughness. The value of the loss coefficient that we measure here is comparable to what we measure on waveguide-integrated synthetic MoS<sub>2</sub> thin films ( $k \approx 0.04 - 0.1$ , unpublished), and approaches our theoretical predictions for ideal, bulk MoS<sub>2</sub> ( $k \approx 0.01 - 0.02$ ).<sup>4,5</sup> These values bode well for refractive, low-loss applications of MoS<sub>2</sub> in integrated photonics.

To estimate oxide thickness from our SE data we turn to modeling. We model our samples as a semi-infinite substrate capped by a thin oxide film. We assume that the oxide is a dielectric with refractive index spectra equal to that of bulk ZrO<sub>2</sub> (using reference data) or thin film MoO<sub>3</sub>.<sup>17</sup> Modeling the SE data in this way is sensitive to oxide thickness down to  $\approx 2$  Å; below this thickness, the model cannot accurately fit the data. 2 Å is comparable to a Mo-O bond length, and therefore it is not accurate to discuss such thin films of MoO<sub>3</sub>. Such modeling results might

represent physical effects such as incomplete oxide coverage, or the chemisorption of oxygen atoms. For further detail on the procedures for modeling and fitting SE data, please see the Supporting Information (SI).

In **Fig. 4a-b** we plot the time-dependence of the growth of native oxide on  $\text{ZrS}_x\text{Se}_{2-x}$  and  $\text{MoS}_2$ . The oxidation of Se-rich  $\text{ZrS}_x\text{Se}_{2-x}$  starts immediately after cleaving and the oxide grows approximately logarithmically in time, showing no sign of stopping within the 160 min observation window. S-rich samples oxidize more slowly; for  $\text{ZrS}_2$  the oxidation process appears to stop above  $\approx 1$  nm of oxide thickness. The logarithmic growth of oxide on  $\text{ZrSe}_2$  suggests a diffusion-limited process, growing as the square-root of time ( $\sqrt{t}$ ). Without further study, we cannot know what species are diffusing across the oxide layer, nor can we know the exact composition of the forming oxide, which is likely a zirconium oxy-sulfide instead of pure  $\text{ZrO}_2$ .<sup>5</sup> These atomistic details are revealed by molecular dynamics (MD) simulations, described below.

We find that  $\text{MoS}_2$  barely oxidizes in air after cleaving, if at all. Our SE modeling and data analysis is consistent with an oxide thickness of  $\approx 1$  Å forming within 5 hrs after cleaving, and remaining stable after 6 days on air exposure, as we show in **Fig. 4b**. However, this result is below the experimental sensitivity, and therefore our data is also consistent with a stable and pristine  $\text{MoS}_2$  surface. To distinguish between these two scenarios – incipient oxidation, or a stable and pristine  $\text{MoS}_2$  surface – we turn to XPS. As we show in **Fig. 4c**, the O 1s spectrum shows no detectable Mo-O bonding (530.2 eV for  $\text{MoO}_3$ ), and the S 2p spectrum shows no S-O bonding (167 eV for  $\text{SO}_2$ ), indicating that the  $\text{MoS}_2$  surface is not oxidized. These XPS results were obtained from a geological  $\text{MoS}_2$  crystal that was mechanically cleaved and then exposed to ambient conditions for a year. Both SE and XPS show that the surface of  $\text{MoS}_2$  is stable and non-reactive in typical laboratory conditions. Similarly, Mirabelli *et al.* found that freshly-cleaved

MoS<sub>2</sub> shows no signs of degradation in air, as measured by atomic force microscopy.<sup>13</sup> Although MoS<sub>2</sub> oxidation in air is thermodynamically favorable, stability in ambient conditions has been explained by the slow kinetics of oxygen absorption and dissociation.<sup>15</sup> Oxidation is accelerated at active sites such as vacancies, grain boundaries, and edges.<sup>10,18,19</sup>

To understand the rapid oxidation of Zr-based TMDs compared to MoS<sub>2</sub>, we perform RMD simulations of the oxidation of MoS<sub>2</sub> and ZrS<sub>2</sub> slabs (details below in Methods; further details can be found in the SI). We simulate oxidation in an oxygen partial pressure of 1.16 kbar and at 800 K, to accelerate the process; as a result, the timescales of oxidation observed in simulation are not expected to match those observed in experiment. In **Figs. 5a-b** we show the initial simulation setup (at time  $t = 0$  ns) and the final snapshot ( $t = 2.5$  ns) for MoS<sub>2</sub> oxidation. The simulation box is periodic in the  $\langle 100 \rangle$  and  $\langle 010 \rangle$  directions (*i.e.*, in-plane). We employ a similar setup for simulating ZrS<sub>2</sub> oxidation, as shown in **Fig. 5c-d**.

**Figs. 5a-d** show that ZrS<sub>2</sub> oxidizes extensively compared to MoS<sub>2</sub>. To quantify the extent of oxidation, we show in **Figs. 5e-f** the total numbers of M-S, M-O, O-O, and S-O bonds (M = Mo or Zr). The increase in Mo-O with oxidation time is negligible compared to the rapid increase of Zr-O bonds. Concurrently, we observe a notable decrease in O-O bonds in the ZrS<sub>2</sub> simulation, suggesting scission of O-O bonds followed by formation of Zr-O bonds. The bond counting data in **Fig. 5f** suggest that ZrS<sub>2</sub> oxidation progresses in two stages. During the first 0.1 ns, the number of Zr-O bonds rises rapidly, followed by much slower increase at longer times. The rapid initial reaction may be explained by energetically-favored O<sub>2</sub> adsorption on the ZrS<sub>2</sub> surface.<sup>20</sup> The rapid increase in the number of Zr-O bonds is not accompanied by a similarly rapid decrease in the number of Zr-S bonds, as we discuss below. The subsequent, slower process of Zr-O bond formation represents the growth of an amorphous oxy-sulfide that largely eliminates the vdW gaps.



In contrast, we observe almost no decrease of O-O bonds in the MoS<sub>2</sub> simulation. This suggests that MoS<sub>2</sub> remains mostly inert and stable in the simulated environment.

We analyze the process of ZrS<sub>2</sub> oxidation in detail by considering atomic trajectories. We find that oxidation proceeds in six steps: (1) adsorption of O<sub>2</sub> molecules on the ZrS<sub>2</sub> surface; (2) dissociation of O<sub>2</sub> on ZrS<sub>2</sub> surface, and formation of Zr-O bonds; (3) Zr pushed into vdW gaps between TMD layers, due to formation of new Zr-O bonds; (4) formation of inter-layer Zr-S and Zr-O bonds, resulting in breakdown of the layered crystal structure; (5) oxygen transport laterally within and vertically between layers by a mechanism of Zr-O bond switching; (6) formation and out-diffusion of SO<sub>2</sub>. In **Fig. 6a-b** we show the cross-section and top-down view of the simulation at  $t = 2$  ps, illustrating steps 1-2. We indicate O<sub>2</sub> adsorption sites with black rectangles. We find that the adsorption of O<sub>2</sub> on the ZrS<sub>2</sub> basal surface is energetically-favorable, with adsorption energy  $E_{\text{ads}} = -0.006$  eV per O<sub>2</sub> molecule, which we calculate by density function theory (DFT) simulations of a ZrS<sub>2</sub> surface-O<sub>2</sub> molecule system. In contrast, we find no stable, relaxed energetic minimum for a MoS<sub>2</sub> surface-O<sub>2</sub> molecule system, indicating that the adsorption energy is positive. Constrained MD simulations paint a similar picture, that O<sub>2</sub> adsorption is favorable on ZrS<sub>2</sub> but unfavorable on MoS<sub>2</sub> (see **Fig. S3**). After rapid adsorption of O<sub>2</sub>, we observe O-O bond breaking and the formation of Zr-O bonds. We also observe 2- and 3-coordinated oxygen atoms on the ZrS<sub>2</sub> surface after O-O bond breakage, corresponding to 2-coordinated bridge oxygen, and 3-coordinated oxygen that are seeds for zirconia growth. A similar process was proposed for the oxidation of monolayer ZrS<sub>2</sub>.<sup>21</sup>

Following the initial formation of Zr-O bonds, Zr moves from the top layer into the interlayer region. The protrusion of Zr atoms results in the collapse of the vdW gap between ZrS<sub>2</sub> layers by the formation of new, interlayer Zr-S and Zr-O bonds, resulting in amorphous, non-layered

material. This is illustrated by a simulation view at  $t = 2.5$  ns, presented in **Fig. 6c-d**. The close-up in **Fig. 6d** highlights the inter-layer Zr atoms and bonds. The expansion of these disordered regions into the vdW gaps provides pathways for oxygen transport further into the  $\text{ZrS}_2$  crystal. We find that oxygen transport proceeds by a process of Zr-O bond switching, illustrated step-by-step in **Fig. 6e**, in which Zr and O atoms are numbered and S atoms are omitted for clarity. The coordination of oxygen atom O1 first changes from 3 to 2 by the breakage of the Zr1-O1 bond. The subsequent creation of a new Zr4-O1 bond restores the 3-fold coordination. A similar process continues when the Zr2-O1 bond is broken and a new Zr5-O1 bond is formed. Oxygen thus traverses the system by successive breaking and forming Zr-O bonds. This bond-switching mechanism for oxygen transport is akin to Grotthuss mechanism which plays essential roles in various processes in oxides.<sup>22-24</sup> It is notable that the process of Zr-O bond switching and oxygen transport is not correlated with a decrease in the number of Zr-S bonds. This suggests that S atoms act as spectators during these initial steps of Zr-O bond formation, amorphization, and oxygen transport, and that charge neutrality is maintained by successive redox transitions at the S sites. The intermediate phase is therefore a zirconium oxy-sulfide, with mixed-valence sulfur ions. The thermodynamic end-products of  $\text{ZrS}_2$  oxidation are  $\text{ZrO}_2$  and  $\text{SO}_2$ ; therefore, the oxidation state of sulfur goes from  $\text{S}^{2-}$  to  $\text{S}^{4+}$ . It is interesting that the oxidation of sulfur is mediated initially through the Zr site. These processes are also observed in first-principles QMD simulations (**Figs. S4 and S5**), thus validating these atomistic mechanisms of  $\text{ZrS}_2$  oxidation.

The last step in the oxidation of  $\text{ZrS}_2$  is the formation and out-diffusion of  $\text{SO}_2$ . Our simulation at 800 K does not extend for long enough time to observe this process. Simulations performed at a much higher temperature of 1500 K do observe the formation and out-diffusion of  $\text{SO}_2$  molecules

(Fig. S6). We also observe that oxidation is accelerated by the presence of a grain boundary, although the key atomic mechanisms remain similar to the case of a pristine  $\text{ZrS}_2$  slab.

## Conclusions

We find experimentally that the exposed basal surfaces of  $\text{ZrS}_x\text{Se}_{2-x}$  oxidize spontaneously in ambient conditions and on time scales relevant for device processing, and that Se-rich compositions are more unstable than S-rich compositions. Combined with previous reports of oxidation of  $\text{ZrTe}_2$ , these results illustrate a trend of increasing stability on moving from Te-, to Se-, to S-based TMDs.<sup>25</sup> MD simulations reveal that oxidation of  $\text{ZrS}_2$  proceeds by rapid  $\text{O}_2$  adsorption and bond scission, followed by oxygen transport into the crystal via a mechanism of Zr-O bond switching, and the collapse of vdW gaps resulting in an intermediate, amorphous oxy-sulfide. In contrast, we find that the basal surface of  $\text{MoS}_2$  is stable in air and does not form an oxide on laboratory time scales (*e.g.* several weeks of continuous exposure). Our results are limited to the basal plane of single crystals, and to ambient laboratory conditions. It will be interesting to study the oxidation of thin films produced by various methods, especially including wafer-scale processes that will be essential for device fabrication.<sup>4</sup> It will also be interesting to study the oxidation of TMDs in different conditions, such as may be experienced during wafer processing and device fabrication. This is especially pertinent if native oxides are discovered to have beneficial passivating or functional properties, as they do for legacy semiconductors.

## Methods

**Experimental Methods** We study bulk crystals of  $\text{ZrS}_x\text{Se}_{2-x}$  alloys and  $\text{MoS}_2$ .  $\text{ZrS}_x\text{Se}_{2-x}$  crystals spanning the full composition range from  $\text{ZrS}_2$  ( $x = 0$ ) to  $\text{ZrS}_2$  ( $x = 2$ ) are obtained by chemical

vapor transport synthesis in sealed quartz ampoules using high-purity sulfur and selenium powders mixed with zirconium lump pieces. Iodine was employed as a transport agent at a concentration of  $5 \text{ mg/cm}^3$  to facilitate the growth of cm-scale flakes. The chalcogenide source molar stoichiometry was varied to control the alloy composition. The  $\text{ZrS}_x\text{Se}_{2-x}$  binary system is isomorphic and forms a full solid solution in the 1T structure (space group:  $\text{P}\bar{3}\text{m1}$  #164).<sup>26</sup> We study naturally-occurring  $\text{MoS}_2$  crystals (2H structure, space group:  $\text{P}6_3/\text{mmc}$  #194) received from the Smithsonian Institution (catalog number NMNH B3306). In **Fig. 1a** we show photographs of several of the crystals studied.

We use adhesive tape (3M, Scotch) to create newly-exposed and oxide-free surfaces by mechanical cleaving. We affix the freshly-cleaved crystals on the tape to a glass slide for inspection. We then use SE to monitor the native oxidation process as a function of time, from minutes to days. The entire process, from mechanical cleaving to SE measurements, is performed in typical laboratory ambient conditions: temperature  $\sim 20 \text{ }^\circ\text{C}$ , and relative humidity  $\sim 50\%$ .

SE is a powerful method for semiconductor and dielectric thin film metrology, and is proven for characterizing the native oxide of silicon.<sup>27</sup> Our previous study on sulfur-based TMDs found that SE is also sensitive to the native oxides in these materials, and therefore can be used to monitor oxide formation.<sup>5</sup> We perform SE measurements using a UV-NIR Vase ellipsometer from J. A. Woollam in the photon energy range 1.25 to 6.5 eV (wavelength range 992 to 190 nm). However, we only report results between 1.25 and 5 eV, due to large depolarization outside of this range. This ellipsometer uses an automatic rotating analyzer and an auto-retarder. We use focusing optics to generate a measurement spot approximately  $300 \mu\text{m}$  in diameter, and we perform all measurements on mirror-smooth surfaces. We carry out all measurements at a fixed angle-of-incidence of  $70^\circ$ . TMDs are highly anisotropic, but also have very large ordinary refractive indices

- they are optically very dense for light propagating perpendicular to the basal plane. As a result, incident light is refracted strongly downward inside the crystals, and our SE measurements are sensitive only to the ordinary refractive index.<sup>5</sup> Our samples are opaque over the photon energy range used in this study, and therefore our data are not affected by scatter from the back surface, which would require special care in analysis.<sup>6</sup>

We complement our SE experiments with X-ray photoelectron spectroscopy (XPS) measurements of an atmosphere-exposed MoS<sub>2</sub> surface. A geological MoS<sub>2</sub> crystal from SPI Supplies is mechanically cleaved and kept in a sample container. After a year in atmosphere, XPS spectra of the MoS<sub>2</sub> surface are obtained using a monochromated Al K $\alpha$  X-ray source (1486.7 eV) at 300 W and a Scienta Omicron R3000 analyzer at a pass energy of 50 eV. The ultra-high vacuum system for XPS characterization used in this work is described elsewhere.<sup>28</sup>

***Theory and simulation methods*** We perform RMD simulations based on the ReaxFF reactive force field to study the oxidation of ZrS<sub>2</sub> and MoS<sub>2</sub> slabs.<sup>29,30</sup> A ReaxFF parameter set for Mo/O/S interactions in the MoS<sub>2</sub> oxidation was taken from Hong *et al.*<sup>31</sup> Another ReaxFF parameter set for Zr/O interactions was successfully developed by van Duin *et al.*<sup>32</sup> We then merged these two parameter sets into a single force field. We further developed this force field for Zr/O/S interactions by comparing with quantum mechanical (QM) calculations. Our newly-developed Mo/Zr/O/S force field can be found in the SI. The SI also includes the validation of the Mo/Zr/O/S force field against QM data sets and QMD simulations. We perform RMD simulations in the canonical (NVT) ensemble, where the temperature is controlled by a Nose-Hoover thermostat, with a temperature-damping constant of 100 fs.<sup>33,34</sup> We numerically integrate the equations of motion with a time step of 1 fs. The lateral dimensions of the MoS<sub>2</sub> simulation cell are 46.83  $\times$  40.36 Å<sup>2</sup>, and the simulated system contains 4 monolayers of MoS<sub>2</sub> stacked vertically. Similarly, the lateral dimensions of the

ZrS<sub>2</sub> simulation cell are  $53.52 \times 46.35 \text{ \AA}^2$ , and the simulation cell contains 4 monolayers of ZrS<sub>2</sub>. The two outer layers are exposed to O<sub>2</sub> gas. We apply periodic boundary conditions in the lateral directions. Each simulation contains 768 metal atoms (Mo or Zr) and 1536 S atoms, to which we add 2000 O<sub>2</sub> molecules.

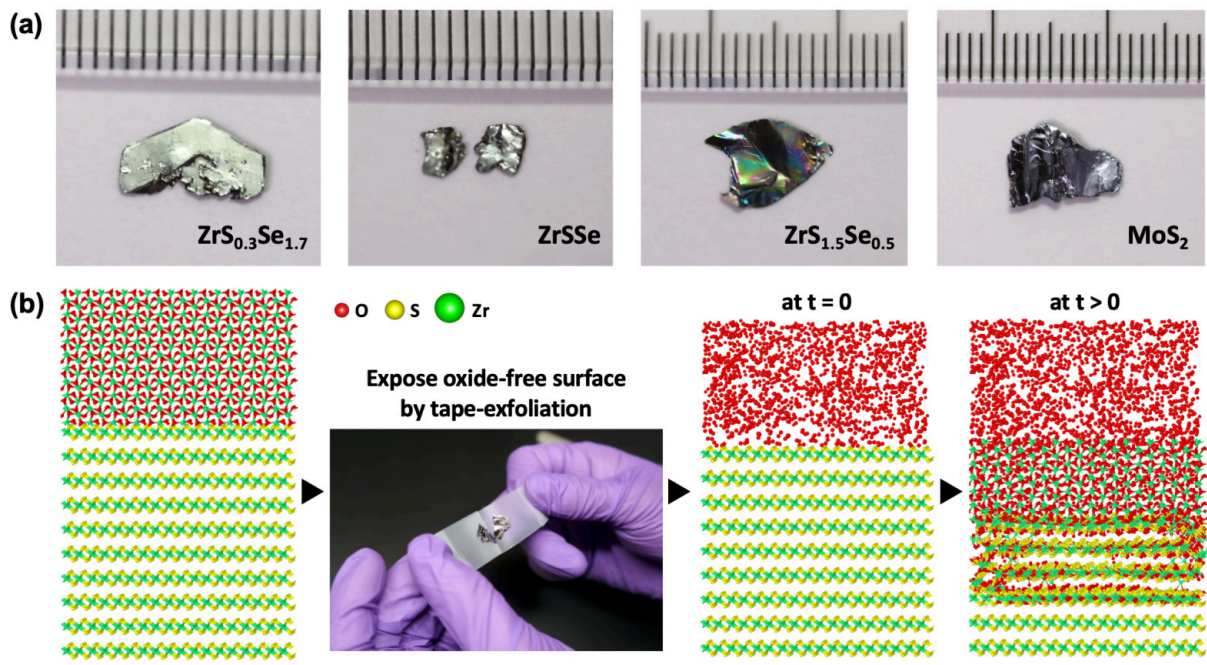


**Figure 1:** (a) Photographs of select TMD bulk crystals used in this study; ruler gradation = 1 mm.

(b) Illustration of tape-time processing for oxidation rate measurements, shown for 1T-ZrS<sub>2</sub>. SE measurements are performed on the newly-exposed basal plane as it oxidizes.

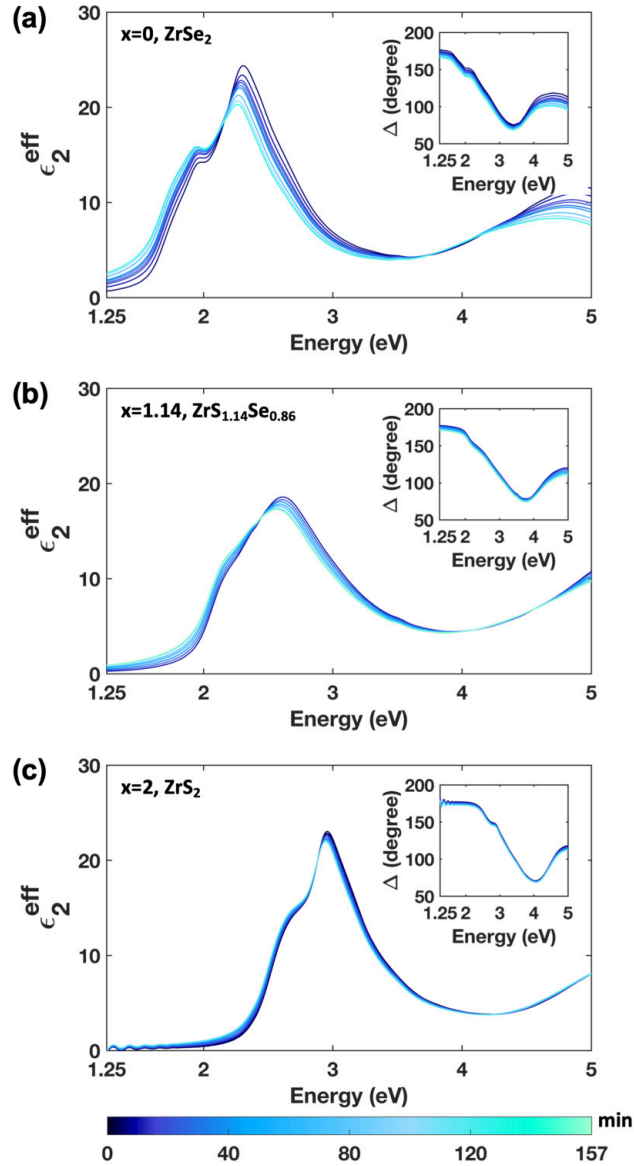


**Figure 2:** Imaginary part of the effective dielectric constant ( $\epsilon_2^{\text{eff}}$ ) measured by SE, as a function of time in ambient conditions after exposing a fresh surface, for three compositions: **(a)**  $\text{ZrSe}_2$ , **(b)**  $\text{ZrS}_{1.14}\text{Se}_{0.86}$ , **(c)**  $\text{ZrS}_2$ . The insets show the SE amplitude ( $\Delta$ , units: degrees) for the same data series. The color bar at the bottom indicates the exposure time after cleaving.



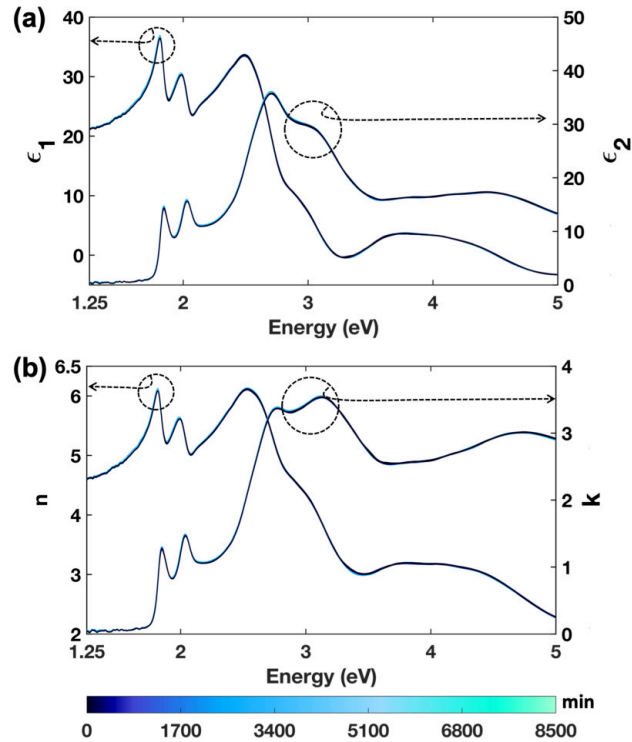


**Figure 3:** Complex dielectric constant **(a)** and refractive index **(b)** of MoS<sub>2</sub> determined by SE measurements on a freshly-cleaved surface. The color series indicates the time elapsed between cleaving the surface and taking the SE data. The spectra recorded at times between 6 and 8,498 min overlap and are barely distinguishable. This time-invariance suggests that the freshly-exposed MoS<sub>2</sub> surface is stable in air on laboratory time scales.

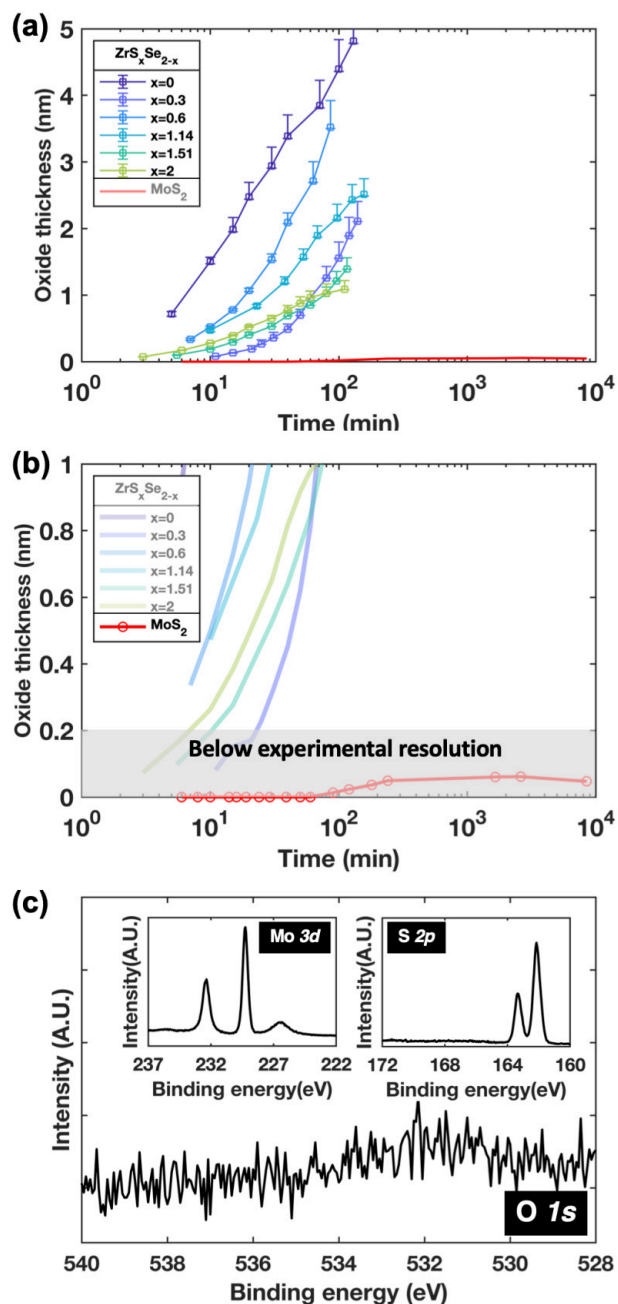


**Figure 4:** Rate of native oxide formation on freshly-cleaved  $ZrS_xSe_{2-x}$  and  $MoS_2$ . (a) Oxide thickness vs. exposure time for  $ZrS_xSe_{2-x}$  alloys; from blue to light green,  $x=0$ ,  $x=0.3$ ,  $x=0.6$ ,  $x=1.14$ ,  $x=1.51$ ,  $x=2$ . The error bars represent systematic errors in the model and nonlinear regression procedure: 10% error in the oxide surface roughness, and 5% error in the regression starting parameters. (b) Plot of oxide thickness vs. exposure time for  $MoS_2$ . The model-based data

analysis infers an oxide thickness that is below the experimental resolution of  $\approx 2 \text{ \AA}$ , which is indicated by the grey region. (c) XPS O-1s peak and (inset) Mo-3d peak and S-2p peak for a MoS<sub>2</sub> crystal stored in laboratory ambient conditions for a year after cleaving. No oxygen signal is detected.

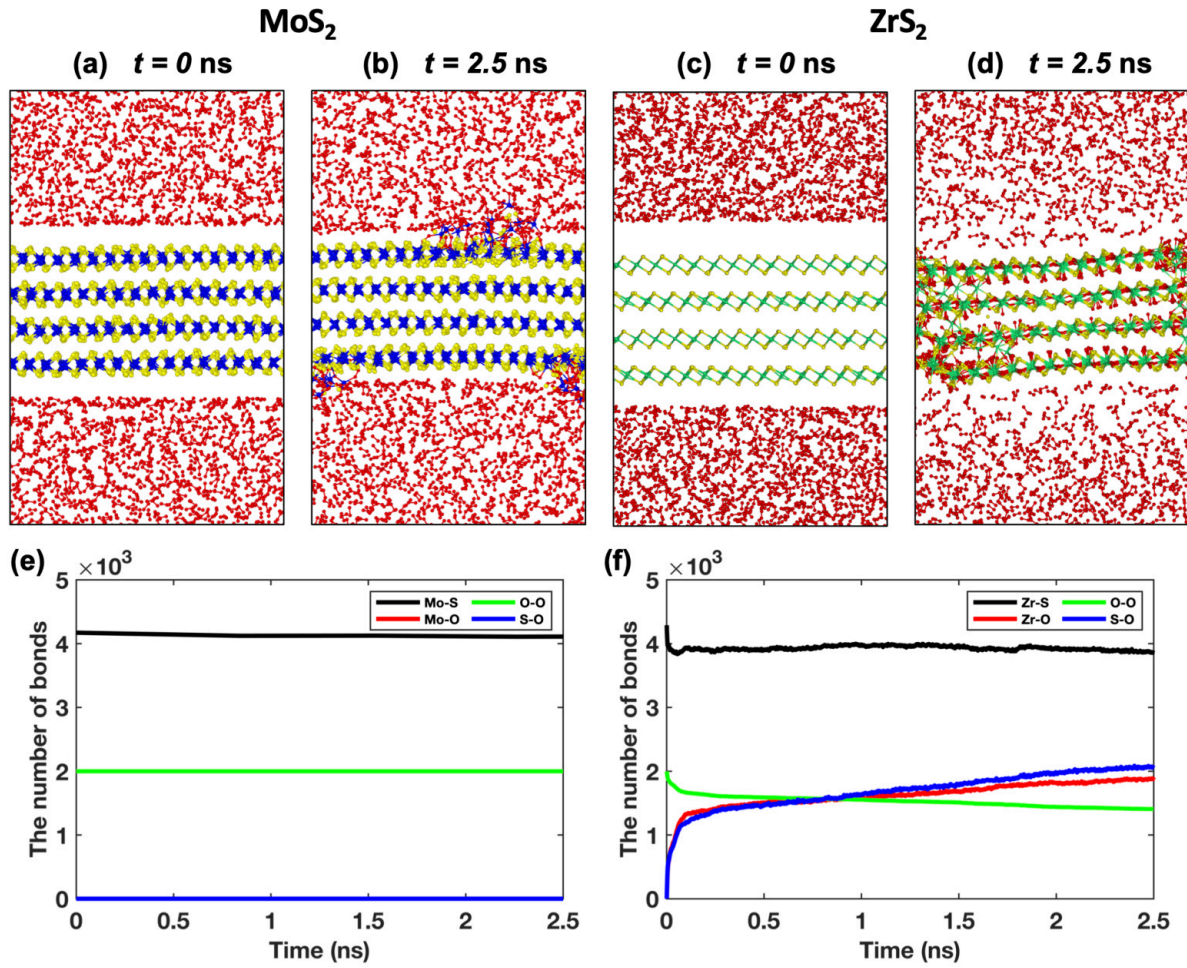


**Figure 5:** RMD simulations of MoS<sub>2</sub> and ZrS<sub>2</sub> oxidation. Snapshots of (a-b) MoS<sub>2</sub> oxidation and (c-d) ZrS<sub>2</sub> oxidation at time  $t = 0$  and 2.5 ns, respectively. Spheres represent individual atoms: blue (Mo), green (Zr), yellow (S) and red (O). Time evolution of corresponding bond count for (e) MoS<sub>2</sub> and (f) ZrS<sub>2</sub> oxidation.

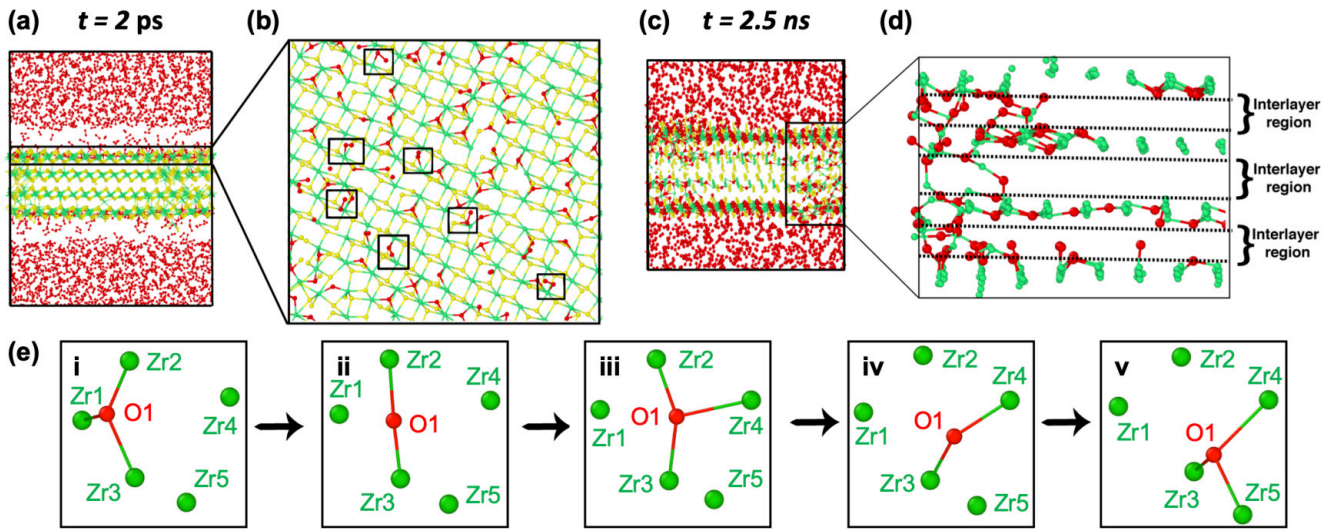


**Figure 6:** Atomistic mechanisms of ZrS<sub>2</sub> oxidation. Cross section (a) and top-down (b) views at  $t = 2$  ps, showing O<sub>2</sub> adsorption and Zr-O bond formation that involves both 2- and 3-fold coordinated oxygen atoms (enclosed by black rectangles). Cross section (c) and close-up (d) view at  $t = 2.5$  ns, showing the formation of an amorphous matrix and the closing of the vdW gaps; S atoms are not shown in (d) for clarity. (e) Oxygen transport mechanism of Zr-O bond switching, including oxygen switching between 2- and 3-fold coordination: (i-ii) breakage of Zr1-O1 bond and decrease in coordination number (3 $\rightarrow$ 2); (ii-iii) formation of Zr4-O1 bond and increase in coordination number (2 $\rightarrow$ 3); (iii-iv) breakage of Zr2-O1 bond and reduced coordination number (3 $\rightarrow$ 2); (iv-5) formation of Zr5-O1 bond and coordination number recovery (2 $\rightarrow$ 3).

## Acknowledgements

This work was supported by an Office of Naval Research MURI through grant #N00014-17-1-2661. We acknowledge the use of facilities and instrumentation supported by NSF through the Massachusetts Institute of Technology (MIT) Materials Research Science and Engineering Center DMR - 1419807. This material is based upon work sponsored in part by the U.S. Army Research Office through the Institute for Soldier Nanotechnologies, under contract number W911NF-13-D-0001. The work at USC was supported as part of the Computational Materials Sciences Program funded by the U.S. Department of Energy, Office of Science, Basic Energy Sciences, under Award Number DE-SC0014607. We would also like to thank USC High Performance Computing Center for provided computing resources. The work was financially supported by the National Science Foundation (NSF) through the Pennsylvania State University 2D Crystal Consortium – Materials Innovation Platform (2DCC-MIP) under NSF cooperative agreement DMR-1539916. P.M. Vora and S.M. Oliver acknowledge support from the George Mason University Quantum Materials Center, Presidential Scholars Program, and from the NSF through Grant No. 1847782. We acknowledge assistance from the Department of Mineral Sciences, Smithsonian Institution. M.G.S. acknowledges support through the William L. Ballard Jr. Endowed Graduate Fellowship.

**Supporting Information Available.** The following files are available for free of charge.

S1. Optical modelling – oxide and surface roughness; S2. ReaxFF reactive force field development for the Zr/S interactions; S3. O<sub>2</sub> adsorption energy on MoS<sub>2</sub> and ZrS<sub>2</sub> surfaces by quantum-mechanical calculation; S4. Validation of ZrS<sub>2</sub> force field by quantum molecular dynamics simulation; S5. ZrS<sub>2</sub> oxidation at 1500 K (PDF).

A ReaxFF parameter set for Mo/Zr/S/O interactions (TXT)

## AUTHOR INFORMATION

### Corresponding Author

E-mail: [rjaramil@mit.edu](mailto:rjaramil@mit.edu)

### Present Addresses

† Present address: Department of Physics, Indian Institute of Science, Bengaluru, Karnataka, 560012, India

## REFERENCES

- (1) Jariwala, D.; Sangwan, V. K.; Lauhon, L. J.; Marks, T. J.; Hersam, M. C. Emerging Device Applications for Semiconducting Two-Dimensional Transition Metal Dichalcogenides. *ACS Nano* 2014, 8, 1102–1120.
- (2) Wang, Q. H.; Kalantar-Zadeh, K.; Kis, A.; Coleman, J. N.; Strano, M. S. Electronics and Optoelectronics of Two-Dimensional Transition Metal Dichalcogenides. *Nature Nanotech* 2012, 7, 699–712.
- (3) McDonnell, S. J.; Wallace, R. M. Atomically-Thin Layered Films for Device Applications Based upon 2D TMDC Materials. *Thin Solid Films* 2016, 616, 482–501.
- (4) Jo, S. S.; Li, Y.; Singh, A.; Kumar, A.; Frisone, S.; LeBeau, J. M.; Jaramillo, R. Formation of Large-Area MoS<sub>2</sub> Thin Films by Oxygen-Catalyzed Sulfurization of Mo Thin Films. *Journal of Vacuum Science & Technology A* 2020, 38, 013405.
- (5) Singh, A.; Li, Y.; Fodor, B.; Makai, L.; Zhou, J.; Xu, H.; Akey, A.; Li, J.; Jaramillo, R. Near-Infrared Optical Properties and Proposed Phase-Change Usefulness of Transition Metal Disulfides. *Appl. Phys. Lett.* 2019, 115, 161902.

- (6) Li, Y.; Singh, A.; Krylyuk, S.; Davydov, A.; Jaramillo, R. Near-Infrared Photonic Phase-Change Properties of Transition Metal Ditellurides. In *Low-Dimensional Materials and Devices 2019*; Kobayashi, N. P., Talin, A. A., Davydov, A. V., Eds.; SPIE: San Diego, United States, 2019; pp 28.
- (7) Sze, S. M. *Semiconductor Devices: Pioneering Papers*; World Scientific, 1991.
- (8) Gao, J.; Li, B.; Tan, J.; Chow, P.; Lu, T.-M.; Koratkar, N. Aging of Transition Metal Dichalcogenide Monolayers. *ACS Nano* 2016, 10, 2628–2635.
- (9) Ye, F.; Lee, J.; Hu, J.; Mao, Z.; Wei, J.; Feng, P. X.-L. Environmental Instability and Degradation of Single- and Few-Layer WTe<sub>2</sub> Nanosheets in Ambient Conditions. *Small* 2016, 12, 5802–5808.
- (10) Sahoo, P. K.; Zong, H.; Liu, J.; Xue, W.; Lai, X.; Gutiérrez, H. R.; Voronine, D. V. Probing Nano-Heterogeneity and Aging Effects in Lateral 2D Heterostructures Using Tip-Enhanced Photoluminescence. *Opt. Mater. Express* 2019, 9, 1620.
- (11) Su, C.; Yin, Z.; Yan, Q.-B.; Wang, Z.; Lin, H.; Sun, L.; Xu, W.; Yamada, T.; Ji, X.; Zettsu, N. et al., Waterproof Molecular Monolayers Stabilize 2D Materials. *Proc Natl Acad Sci USA* 2019, 116, 20844–20849.
- (12) Szychalski, W. L.; Pisarek, M.; Szoszkiewicz, R. Microscale Insight into Oxidation of Single MoS<sub>2</sub> Crystals in Air. *J. Phys. Chem. C* 2017, 121, 26027–26033.
- (13) Mirabelli, G.; McGeough, C.; Schmidt, M.; McCarthy, E. K.; Monaghan, S.; Povey, I. M.; McCarthy, M.; Gity, F.; Nagle, R.; Hughes, G. et al., Air Sensitivity of MoS<sub>2</sub>, MoSe<sub>2</sub>, MoTe<sub>2</sub>, HfS<sub>2</sub>, and HfSe<sub>2</sub>. *Journal of Applied Physics* 2016, 120, 125102.



- (14) Cruz, A.; Mutlu, Z.; Ozkan, M.; Ozkan, C. S. Raman Investigation of the Air Stability of 2H Polytype HfSe<sub>2</sub> Thin Films. *MRC* 2018, 8, 1191–1196.
- (15) Kc, S.; Longo, R. C.; Wallace, R. M.; Cho, K. Surface Oxidation Energetics and Kinetics on MoS<sub>2</sub> Monolayer. *Journal of Applied Physics* 2015, 117, 135301.
- (16) Oliver, S. M.; Fox, J. J.; Hashemi, A.; Singh, A.; Cavalero, R. L.; Yee, S.; Snyder, D. W.; Jaramillo, R.; Komsa, H.-P.; Vora, P. M. Phonons and Excitons in ZrSe<sub>2</sub>–ZrS<sub>2</sub> Alloys. *J. Mater. Chem. C* 2020, 8, 5732–5743.
- (17) Vos, M. F. J.; Macco, B.; Thissen, N. F. W.; Bol, A. A.; Kessels, W. M. M. (Erwin). Atomic Layer Deposition of Molybdenum Oxide from (NtBu)<sub>2</sub> (NMe<sub>2</sub>)<sub>2</sub> Mo and O<sub>2</sub> Plasma. *Journal of Vacuum Science & Technology A: Vacuum, Surfaces, and Films* 2016, 34, 01A103.
- (18) Liu, H.; Han, N.; Zhao, J. Atomistic Insight into the Oxidation of Monolayer Transition Metal Dichalcogenides: From Structures to Electronic Properties. *RSC Adv.* 2015, 5, 17572–17581.
- (19) Li, Q.; Zhou, Q.; Shi, L.; Chen, Q.; Wang, J. Recent Advances in Oxidation and Degradation Mechanisms of Ultrathin 2D Materials under Ambient Conditions and Their Passivation Strategies. *J. Mater. Chem. A* 2019, 7, 4291–4312.
- (20) Li, Q.; Zheng, S.; Pu, J.; Sun, J.; Huang, L.-F.; Wang, L.; Xue, Q. Thermodynamics and Kinetics of an Oxygen Adatom on Pristine and Functionalized Graphene: Insight Gained into Their Anticorrosion Properties. *Phys. Chem. Chem. Phys.* 2019, 21, 12121–12129.

- (21) Li, Q.; Shi, L.; Wu, R.; Lin, C.; Bai, X.; Ouyang, Y.; Baraiya, B. A.; Jha, P. K.; Wang, J. Unveiling Chemical Reactivity and Oxidation of 1T-Phased Group VI Disulfides. *Phys. Chem. Chem. Phys.* 2019, 21, 17010–17017.
- (22) Nomura, K.; Chen, Y.-C.; Kalia, R. K.; Nakano, A.; Vashishta, P. Defect Migration and Recombination in Nanoindentation of Silica Glass. *Appl. Phys. Lett.* 2011, 99, 111906.
- (23) Shimojo, F.; Ohmura, S.; Kalia, R. K.; Nakano, A.; Vashishta, P. Molecular Dynamics Simulations of Rapid Hydrogen Production from Water Using Aluminum Clusters as Catalyzers. *Phys. Rev. Lett.* 2010, 104, 126102.
- (24) Agmon, N. The Grotthuss Mechanism. *Chemical Physics Letters* 1995, 244, 456–462.
- (25) Mleczko, M. J.; Zhang, C.; Lee, H. R.; Kuo, H.-H.; Magyari-Köpe, B.; Moore, R. G.; Shen, Z.-X.; Fisher, I. R.; Nishi, Y.; Pop, E. HfSe<sub>2</sub> and ZrSe<sub>2</sub>: Two-Dimensional Semiconductors with Native High-k Oxides. *SCIENCE ADVANCES* 2017, 3, e1700481.
- (26) Bartwal, K. S.; Srivastava, O. N. Growth and Characterization of Single Crystals in the Series ZrS<sub>x</sub>Se<sub>2-x</sub>. *Materials Science and Engineering: B* 1995, 33, 115–121.
- (27) Morita, M.; Ohmi, T.; Hasegawa, E.; Kawakami, M.; Ohwada, M. Growth of Native Oxide on a Silicon Surface. *J. Appl. Phys.* 1990, 68, 1272.
- (28) Freedy, K. M.; Litwin, P. M.; McDonnell, S. J. (Invited) In-Vacuo Studies of Transition Metal Dichalcogenide Synthesis and Layered Material Integration. *ECS Transactions* 2017, 77, 11–25.

- (29) Senftle, T. P.; Hong, S.; Islam, M. M.; Kylasa, S. B.; Zheng, Y.; Shin, Y. K.; Junkermeier, C.; Engel-Herbert, R.; Janik, M. J.; Aktulga, H. M. et al., The ReaxFF Reactive Force-Field: Development, Applications and Future Directions. *npj Computational Materials* 2016, 2, 15011.
- (30) van Duin, A. C. T.; Dasgupta, S.; Lorant, F.; Goddard, W. A. ReaxFF: A Reactive Force Field for Hydrocarbons. *J. Phys. Chem. A* 2001, 105, 9396–9409.
- (31) Hong, S.; Sheng, C.; Krishnamoorthy, A.; Rajak, P.; Tiwari, S.; Nomura, K.; Misawa, M.; Shimojo, F.; Kalia, R. K.; Nakano, A.; Vashishta, P. Chemical Vapor Deposition Synthesis of MoS<sub>2</sub> Layers from the Direct Sulfidation of MoO<sub>3</sub> Surfaces Using Reactive Molecular Dynamics Simulations. *J. Phys. Chem. C* 2018, 122, 7494–7503.
- (32) van Duin, A. C. T.; Merinov, B. V.; Jang, S. S.; Goddard, W. A. ReaxFF Reactive Force Field for Solid Oxide Fuel Cell Systems with Application to Oxygen Ion Transport in Yttria-Stabilized Zirconia. *J. Phys. Chem. A* 2008, 112, 3133–3140.
- (33) Nosé, S. A Unified Formulation of the Constant Temperature Molecular Dynamics Methods. *J. Chem. Phys.* 1984, 81, 511–519.
- (34) Hoover, W. G. Canonical Dynamics: Equilibrium Phase-Space Distributions. *Phys. Rev. A* 1985, 31, 1695–1697.